Journal of Volcanology and Geothermal Research 187 (2009) 261–271

Contents lists available at ScienceDirect

Journal of Volcanology and Geothermal Research

journal homepage: www.elsevier.com/locate/jvolgeores

Seismogenic stress field beneath the Tatun Volcano Group, northern Taiwan

K.I. Konstantinou [a,*], C.H. Lin [b], W.T. Liang [b], Y.C. Chan [b]

[a] Institute of Geophysics, National Central University, Jhongli, 320 Taiwan
[b] Institute of Earth Sciences, Academia Sinica, P.O. Box 1-55, Taipei, 115 Taiwan

ARTICLE INFO

Article history:
Received 15 April 2009
Accepted 15 September 2009
Available online 1 October 2009

Keywords:
stress field
stress inversion
crustal anisotropy
Tatun
Taiwan

ABSTRACT

The Tatun Volcano Group (TVG) represents the main volcanic center in northern Taiwan and based on various observations it is considered a potentially active volcano. TVG has been monitored since 2003 by a seismic network that consists of eight stations equipped with three-component, short-period and broadband seismometers. In this study, we use waveform data of high frequency earthquakes in order to investigate the stress field orientation beneath the TVG area. The focal mechanisms of 35 selected events have been derived using P-wave polarities and amplitude ratios, assuming a double-couple source. These fault plane solutions and various subsamples derived from them, were subsequently inverted for the best fitting stress tensor using a linear inversion method. The results show stress homogeneity beneath TVG for depths larger than 3 km while the stress tensor is characterized by a subvertical σ_1 and a subhorizontal NW-SE trending σ_3 axis consistent with the regional stress field in northern Taiwan. On the other hand, Chihsinshan which is an area of vigorous hydrothermal activity, exhibits a localized stress field with horizontal NW-SE trending σ_3 axis and NE–SW trending horizontal σ_1. Such an axes orientation is likely to be causing opening of microcracks and thus favour the ascent and circulation of fluids in the upper crust. Shear wave splitting measurements seem to confirm these results, showing fast polarization directions along NNE–NE, subparallel to the main fracture system in TVG. Shear wave anisotropy averages about 2.9% and is probably caused by an anisotropic volume of fluid-saturated cracks within the upper 2.5 km of the crust.

1. Introduction

The northern part of Taiwan is influenced by two geodynamic processes, namely an active subduction and its corresponding backarc opening. The Ryukyu subduction zone was formed from the oblique movement of the Philippine Sea plate underneath the Eurasian plate at a present rate of 8.2 cm yr^{-1} (Yu et al., 1997) (Fig. 1a). This subduction system extends from Kyushu island in the north following initially a NE–SW direction, to Taiwan in the south, where this direction changes to E–W possibly because of the collision between the Luzon Arc and the Chinese continental shelf (Tsai, 1986; Wu et al., 1997 and references therein). To the north of the subduction, the Okinawa Trough is the backarc basin of the Ryukyu trench and is in the process of opening, as has been demonstrated by continuous GPS measurements at the Ryukyu islands and focal mechanisms of earthquakes occurring offshore NE Taiwan that show extensional faulting (Kao and Jian, 2001).

Volcanism in northern Taiwan is believed to be related either to the Ryukyu subduction zone (Teng, 1996), or to the opening of the Okinawa Trough (Wang et al., 1999) and is expressed through a number of Quaternary volcanoes known as the Tatun Volcano Group (hereafter called TVG). TVG is built on a late Tertiary sedimentary basement and is enclosed by two fault systems, the Chinshan and Kanchiao faults (Fig. 1b). The proximity of TVG to Taipei, the capital of Taiwan, has prompted researchers to investigate its potential for future volcanic activity (Yeh et al., 1998; Yang et al., 1999; Song et al., 2000; Kim et al., 2005; Lin et al., 2005; Konstantinou et al., 2007; Lee et al., 2008). Even though radiometric dating suggests that eruptive activity ceased 0.2 Ma ago, the finding of ash deposits younger than 20 ka in the nearby Taipei basin indicates that the possibility of a future eruption cannot be excluded (Chen and Lin, 2002). Additional observations that support this include strong fumarolic activity, swarm-type seismicity and gas compositions of magmatic origin, as reported in the aforementioned studies. Therefore, even though dormant for the being time, TVG can be considered as potentially active rather than an extinct volcano.

High frequency earthquakes, caused by brittle failure of rock, constitute the largest fraction of the observed seismicity at TVG (Konstantinou et al., 2007). Their occurrence may be attributed either to the regional stress field as the result of plate movements, to stresses induced by the dynamics of a shallow magma chamber, or finally to stresses due to the loading of the volcanic edifice (Cocina et al., 1998; Bianco et al., 1998; Legrand et al., 2002; Moran, 2003; Roman et al., 2004). This study investigates whether seismogenesis at TVG is primarily controlled by regional tectonic or localized fluid-induced stresses. In order to do this we use high-quality, digital waveform data

* Corresponding author. Fax: +886 3 4222044.
E-mail address: kkonst@ncu.edu.tw (K.I. Konstantinou).

0377-0273/$ – see front matter © 2009 Elsevier B.V. All rights reserved.
doi:10.1016/j.jvolgeores.2009.09.011

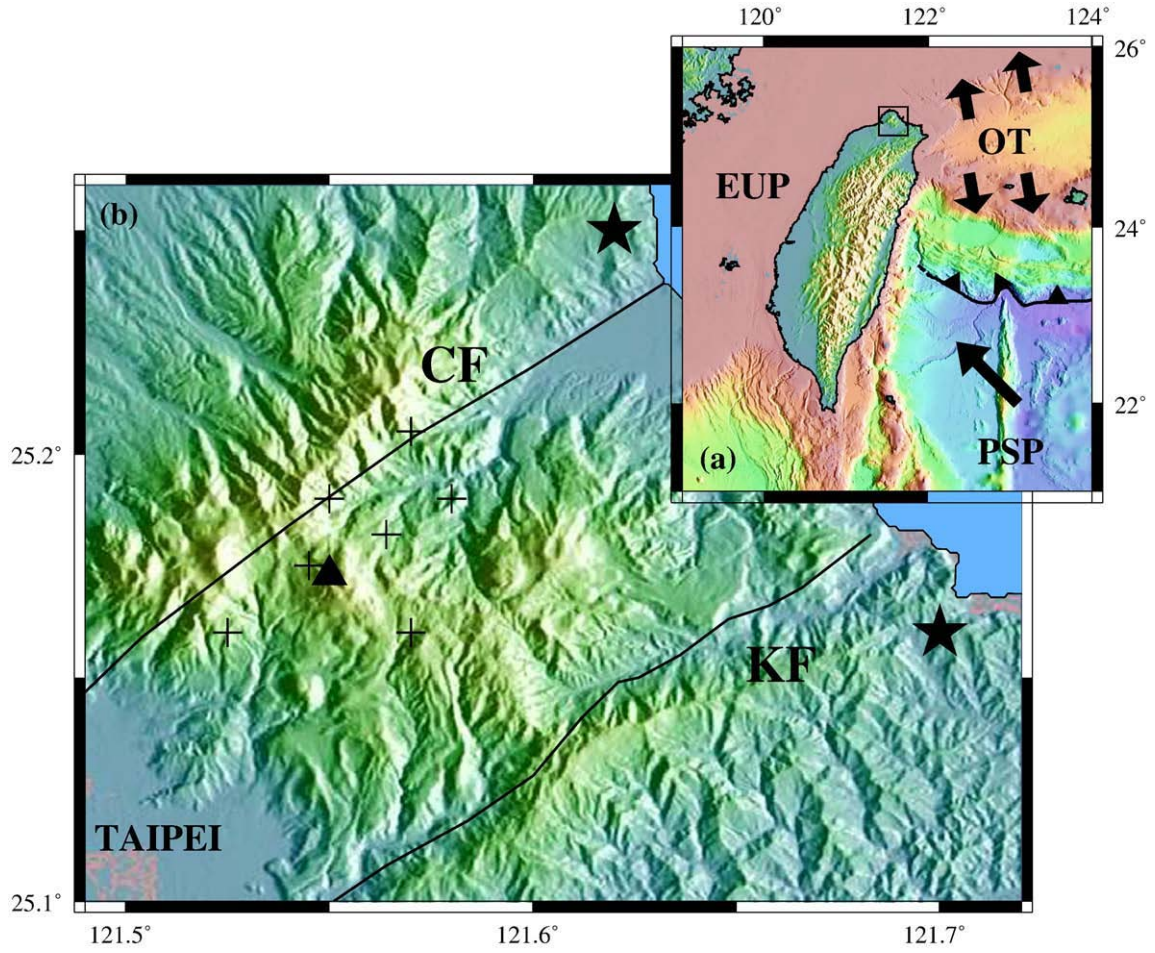

Fig. 1. (a) Map showing the regional tectonic setting and relative motion between the Philippine Sea plate (PSP) and the Eurasian plate (EUP) indicated by an arrow, as well as the opening of the Okinawa Trough (OT) backarc basin. The square in northern Taiwan shows the area of interest. (b) Map showing the area of the Tatun Volcano Group (TVG). The thick line to the south indicates the Kanchiao fault (KF), while that in the north the Chinshan fault (CF). The triangle represents the peak of the Chihsinshan volcanic edifice (height ~1120 m), the crosses indicate the place of hot springs, or fumarole activity after Yang et al. (1999) and the stars show the positions of two nearby nuclear power plants. Part of the Taipei sedimentary basin can be seen at the lower left corner of the map (from Konstantinou et al., 2007). For a coloured version of this figure the reader is referred to the web version of the article.

in an effort to infer the stress field orientation in this volcanic area of northern Taiwan. First, we give a brief overview of the available dataset in terms of waveform characteristics and earthquake locations. This is followed by a description of the estimation of fault plane solutions for a number of selected events and their inversion for the purpose of determining the best-fitting stress tensor. Shear wave anisotropy is an additional source of information about the stress field orientation and we also conduct detailed measurements of splitting parameters. The surface fractures present at the TVG area have been recently mapped using airborn Light Detection And Ranging (LiDAR) data (Chan et al., 2007) and have also been used here to further constrain our results. Lastly, we interpret our findings and discuss their implications for the state of stress and future volcanic activity at TVG.

2. Data and event location

The seismic monitoring of TVG started in May 2003 with the installation of five stations equipped with three-component, short-period sensors. By September 2003 the station number was increased to eight and four of them had both a short-period and a broadband (up to 30 s) sensor (Table 1). The waveform data were recorded at a sampling interval of 100 samples s^{-1} and absolute timing was provided by GPS receivers. The dataset for the period September 2003 until February 2005 has been used in order to classify the recorded seismic signals and to obtain accurate absolute and relative earthquake locations. For more details the interested reader is referred to Konstantinou et al. (2007), thus only a brief summary of these issues will be given here. Seismic signals were classified based on their appearance in the time domain and frequency content into three groups: (a) high frequency events with impulsive P-wave onsets and clear S-wave phases, while most of the energy is concentrated in the band 1–20 Hz; these events may occur individually or as a group the one after the other ('spasmodic burst'), (b) mixed frequency events with sharp P-wave onsets, no clear S-waves consisting of an initial high frequency (up to 40 Hz) part followed by a later low frequency (~5 Hz) harmonic coda, (c) low frequency events in the form of tornillos and monochromatic events of varying duration.

Table 1
List of seismic stations deployed at the TVG area for the period between September 2003 until February 2005.

Station	Lat (°N)	Lon (°E)	Elev (km)	Sensor type
YM01	25.1481	121.5620	0.488	Le3D/CMG-3T
YM02	25.1863	121.5621	0.521	Le3D/CMG-3T
YM03	25.1809	121.5314	0.702	Le3D/CMG-3T
YM04	25.1552	121.5278	0.401	Le3D/CMG-3T
YM05	25.1665	121.5564	0.740	Le3D
YM06	25.1538	121.5943	0.445	Le3D
YM07	25.1771	121.6123	0.456	Le3D
YM08	25.1890	121.5808	0.342	Le3D

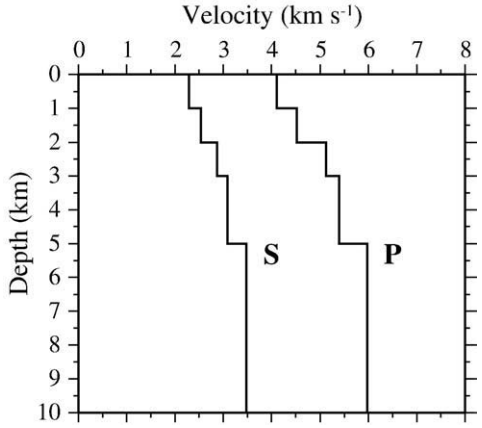

Fig. 2. Diagram showing the minimum 1D P- and S-wave velocity model for the TVG area derived by Konstantinou et al. (2007). The model is well constrained only for the upper 5 km.

The short-period waveforms were used in order to manually pick the arrival times of 144 high frequency events, 59 events belonging to spasmodic bursts and 8 mixed frequency events. Initial locations were obtained using a general 1D velocity model for northern Taiwan and utilizing a probabilistic nonlinear location algorithm (Lomax et al., 2000). Based on these initial locations and P, S travel times a minimum 1D velocity model with station corrections was derived (Fig. 2). Probabilistic nonlinear locations were then recalculated for all picked events using this newly derived velocity model and mean location errors did not exceed 0.7 km horizontally and 1.5 km vertically. A comparison of these locations with relative locations calculated using the double-difference algorithm (Waldhauser and Ellsworth, 2000) showed insignificant differences, implying that the nonlinear probabilistic locations were well-constrained. The location results revealed that high frequency seismicity is concentrated near the Chihsinshan volcanic edifice and the Tayiokeng area where most of the present day hydrothermal activity is observed (Fig. 3). Most events form several tight clusters at depths that range from shallower than 1 to about 4 km. Seismicity in this period manifests itself as swarm activity with an average of 10–15 events per month while the largest recorded event had a local magnitude of 2.83. We chose to restrict our study to the period September 2003–February 2005 for the following reasons: (a) for most of this time all eight stations operated smoothly, unlike later periods when the network experienced several technical problems and (b) accurate locations of high frequency events are already available from our previous study.

3. Focal mechanisms determination

The software package FOCMEC (Snoke et al., 1984) was used in order to determine fault plane solutions of high frequency earthquakes in this study. FOCMEC utilizes polarities of P- and S-waves as well as amplitude ratios (SV/P or SH/P) and performs a systematic grid search for acceptable focal mechanism solutions by assuming that the earthquake source conforms to the double-couple model. In the case when only polarities are used, their consistency is checked with each pair of orthogonal nodal planes. If the number of polarity errors is within a prespecified number, then the solution is accepted. When

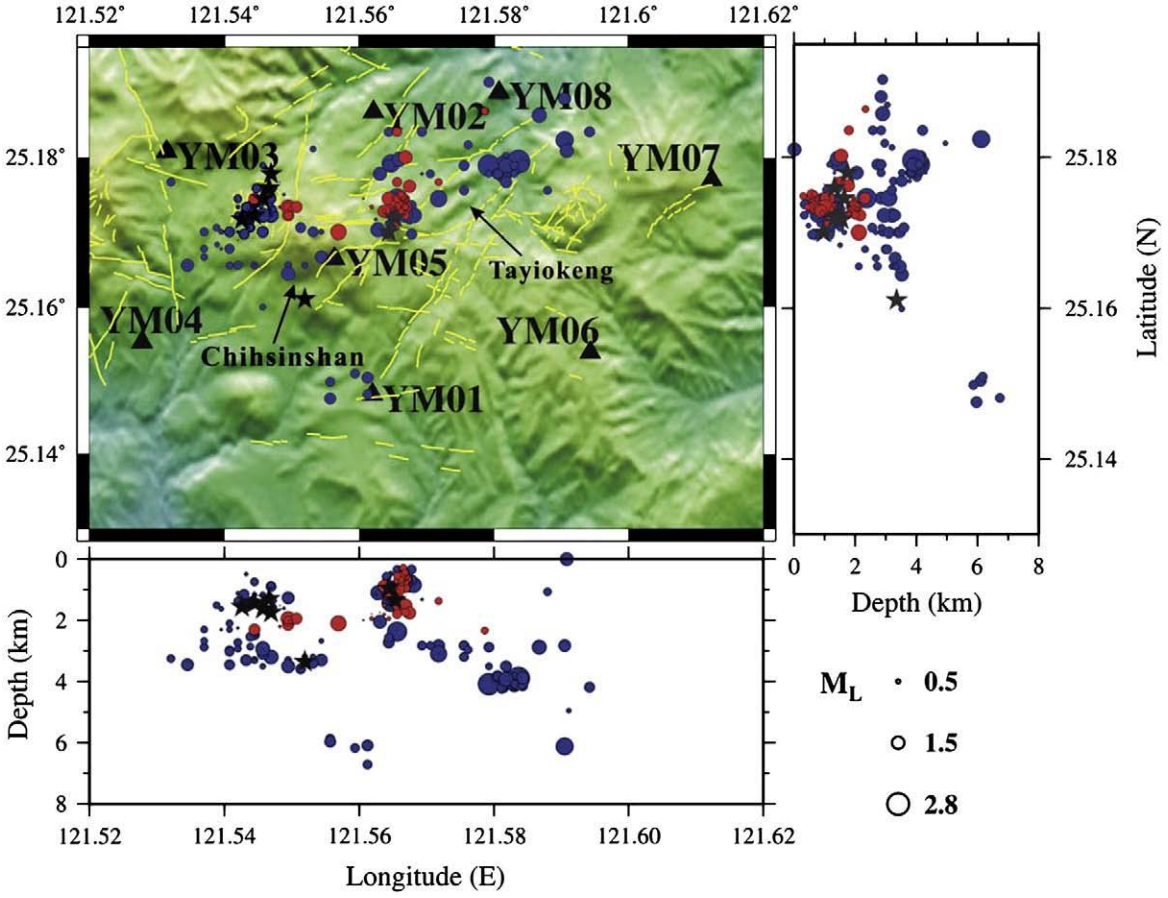

Fig. 3. Map of the TVG area showing the locations obtained using the nonlinear probabilistic algorithm and the minimum 1D model with station corrections (after Konstantinou et al., 2007). The blue circles indicate the isolated high frequency events, the red ones the spasmodic bursts events and the black stars the mixed frequency events. A scale relating the circle size to magnitude values is given at the lower right corner of the plot. The yellow lines are the surface fractures in the TVG area derived from LiDAR data. For a coloured version of this figure the reader is referred to the web version of the article.

amplitude ratios are also included, the difference between the theoretical and observed ones is compared. If the total number of consistent amplitude ratios is within a preset error allowance, then the solution is accepted. The smallest rms error for the acceptable amplitude ratios is used in order to choose the best solution when there are more than one acceptable focal mechanisms.

We initially searched our dataset for the purpose of finding suitable high frequency events for deriving their focal mechanisms. The fact that events belonging to spasmodic bursts usually exhibit a coda that is overlapping with the P-wave onset of the next event makes it very difficult to infer unambiguously first motion polarities. We therefore opted for not using any of these events and instead focused our attention on the remaining 144 high frequency earthquakes. The short-period waveforms of each event were visually inspected in order to check whether a clear P-wave polarity could be observed in at least 7 out of the 8 available stations. Once this requirement was met, the polarities along with the azimuth and takeoff angles for each station (calculated using the minimum 1D velocity model) were input to FOCMEC. A rather crude grid search interval of 5° was chosen, since we are dealing with a relatively small number of observed polarities.

As might be expected, for most of the events this procedure produced a large number of possible solutions that were consistent with each other, but exhibited variations in the strike and/or dip of the nodal planes (Fig. 4a). In these cases the inclusion of amplitude ratios has been shown to greatly improve such poorly constrained focal mechanisms (Hardebeck and Shearer, 2003). In order to avoid problems related to the critical angle and P-to-S conversions, we measure SH/P rather than SV/P amplitude ratios (Rau et al., 1996; Park et al., 2007). First, the short-period waveforms were rotated to the radial-transverse coordinate system with respect to the probabilistic nonlinear location and then lowpass filtered at 5 Hz using a two-pole Butterworth filter. P and SH amplitudes were measured as the maximum zero-to-peak amplitude within the first three half-cycles of the direct arrivals in the vertical and transverse components respectively. These amplitude ratios were corrected first for the free-surface distortion and then for anelastic attenuation effects by using Q_p and Q_s values of 100 and 90 stemming from the attenuation study in northern Taiwan published by Chen et al. (2002). For each event we set a minimum requirement of including at least two amplitude ratios.

After the inclusion of SH/P amplitude ratios the possible focal mechanism solutions have decreased significantly in number and the solution with the smallest rms error was chosen as the best (Fig. 4b, c). In this way we were able to determine focal mechanism solutions for a total of 35 high frequency events. Even though several studies have documented the existence of non-double-couple components for earthquakes occurring in volcanic areas (for a review see Miller et al., 1998), all events we have analyzed were consistent with the double-couple assumption made by FOCMEC. Fig. 5 shows stereographic plots of the resulting 35 focal mechanism solutions (see also Table 2 for more information), while Fig. 6 gives a map view of the distribution of these solutions. It can be seen that all types of faulting are present, however, most of the events seem to have a substantial strike-slip component.

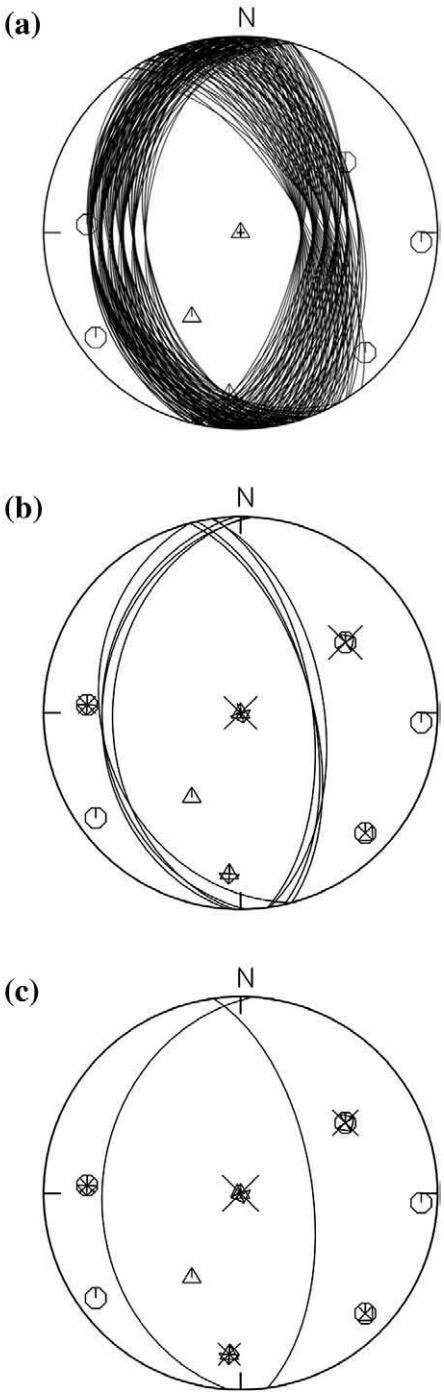

Fig. 4. Upper hemisphere, equal area projections of the focal mechanism solutions derived for an event (M_L 2.20) that occurred at (GMT) 20:09:29.1 September 25, 2003: (a) using only P-wave polarities, (b) using both the P-wave polarities and SH/P amplitude ratios, (c) the solution that had the minimum rms error. The triangles represent stations where the P-wave polarity was a dilatation, while hexagons show stations where the first motion was a compression. The amplitude ratio is proportional to the size of the X symbol that is scaled based on the observed $\log_{10}$(SH/P).

4. Stress tensor inversion

It is expected that for a homogeneous, elastic and isotropic medium without friction and pre-existing fractures, the P and T axes corresponding to the eigen directions of the seismic moment tensor of an earthquake will coincide with the maximum and minimum stress tensor axes, namely σ_1 and σ_3 (e.g., Legrand et al., 2002). However, these simplifying assumptions are seldom valid for real Earth media that are often pre-fractured and of course friction exists on fault surfaces. This implies that the eigen directions of the seismic moment tensor are different from those of the stress tensor and that faults of different orientation may actually correspond to a single stress tensor.

The development of a methodology of how to determine the stress tensor from a set of well-constrained earthquake focal mechanisms has been addressed by several authors previously (Gephart and Forsyth, 1984; Michael, 1984, 1987; Gephart, 1990 among others). Such methodologies are usually based on two assumptions: (a) that earthquakes slip in the direction of the resolved shear stress on the fault plane and (b) the stress field can be considered constant over the space and time scale covered by the dataset. Under these assumptions,

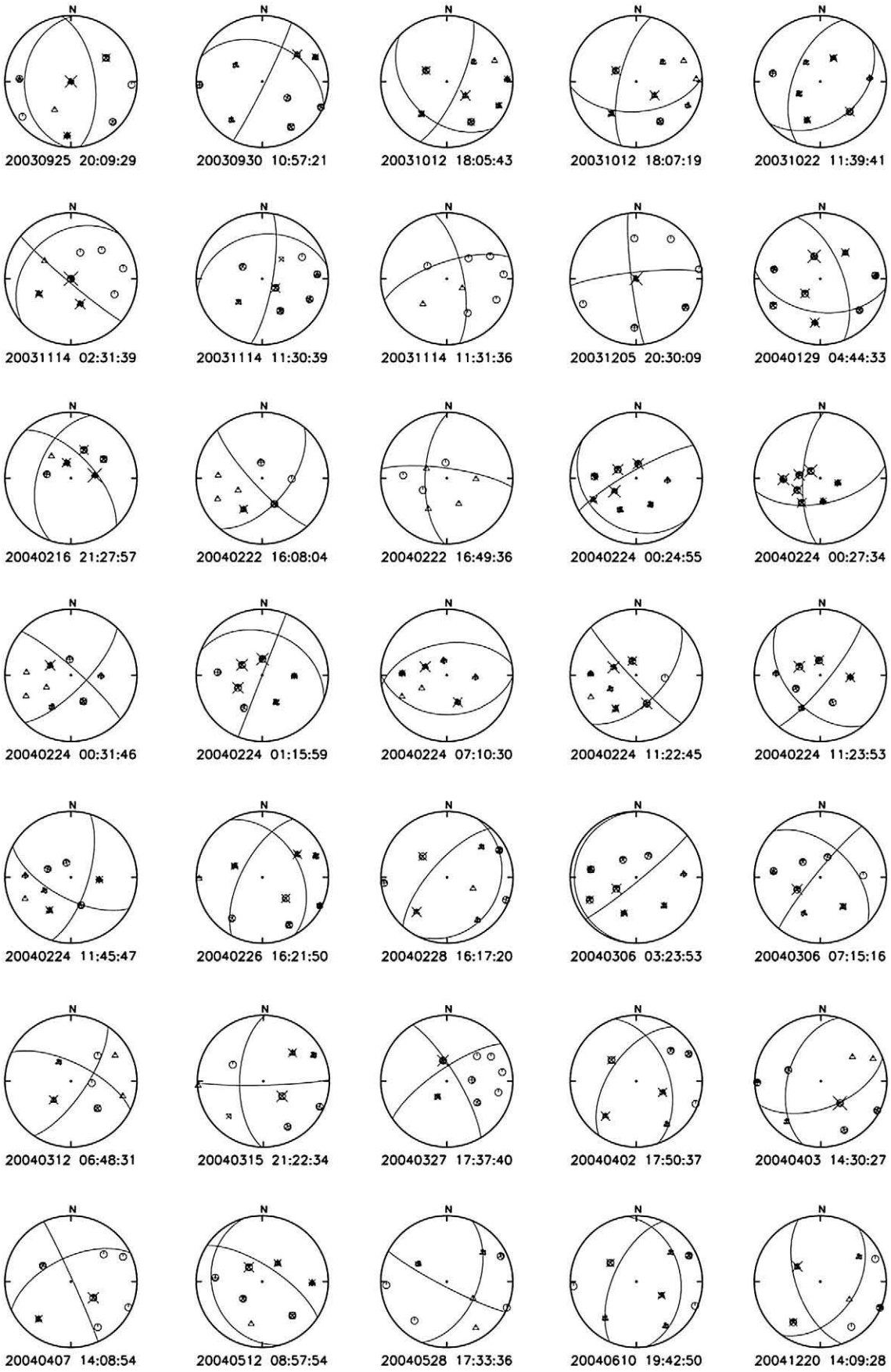

Fig. 5. Upper hemisphere, equal area projections of the fault plane solutions of all 35 events that are considered in this study (see also Table 2 for more details). Symbols are the same as in Fig. 4.

Table 2
Summary of the source parameters and focal mechanisms of the 35 selected events.OT is the origin time, H is the hypocentral depth and M_L is the local magnitude. The fault strike is denoted as ϕ, dip as ξ and rake as λ, while the number signifies the nodal plane (1 or 2).

Date	OT	Lat (°N)	Lon (°E)	H (km)	M_L	ϕ_1	ξ_1	λ_1	ϕ_2	ξ_2	λ_2
20030925	20:09:29.01	25.1793	121.5646	1.4	2.20	172	60	−96	4	30	−80
20030930	10:57:21.83	25.1737	121.5441	1.4	1.38	112	40	−6	206	86	−130
20031012	18:05:43.16	25.1745	121.5444	2.4	1.30	315	40	26	204	74	127
20031012	18:07:19.82	25.1745	121.5444	2.5	0.85	266	52	−26	13	69	−139
20031022	11:39:41.87	25.1745	121.5718	2.8	1.55	231	38	−65	21	56	−108
20031114	02:31:39.73	25.1666	121.5544	3.3	1.60	48	30	7	310	86	120
20031114	11:30:39.35	25.1723	121.5469	3.2	1.80	79	33	−24	190	77	−121
20031114	11:31:36.89	25.1723	121.5457	2.9	1.79	71	69	−22	169	69	−158
20031205	20:30:9.528	25.1703	121.5628	1.1	1.79	353	84	−8	84	82	−174
20040129	04:44:33.99	25.1745	121.5656	2.3	2.41	278	48	39	159	62	130
20040216	21:27:57.64	25.1503	121.5612	6.0	1.42	18	48	−39	137	62	−131
20040222	16:08:4.096	25.1779	121.5817	3.9	1.53	317	79	33	220	57	167
20040222	16:49:36.82	25.1779	121.5817	4.0	1.40	2	63	−14	98	78	−152
20040224	00:24:55.27	25.1790	121.5792	4.0	2.78	306	22	−25	60	81	−110
20040224	00:27:34.56	25.1824	121.5904	6.1	2.17	259	58	−26	3	68	−145
20040224	00:31:46.75	25.1779	121.5817	3.9	1.28	132	82	−18	224	72	−171
20040224	01:15:59.59	25.1779	121.5805	3.8	1.48	201	90	55	111	35	−180
20040224	07:10:30.60	25.1790	121.5830	3.9	2.38	271	40	−82	81	50	−97
20040224	11:22:45.67	25.1796	121.5836	3.9	2.83	317	84	35	223	56	173
20040224	11:23:53.62	25.1790	121.5817	3.9	1.80	319	47	15	219	79	136
20040224	11:45:47.67	25.1790	121.5842	3.8	1.56	298	64	24	197	68	152
20040226	16:21:50.76	25.1759	121.5448	1.4	1.23	151	41	41	28	64	124
20040228	16:17:20.01	25.1714	121.5435	1.4	1.57	42	70	−85	207	21	−104
20040306	03:23:53.84	25.1745	121.5718	3.0	2.03	5	7	45	230	85	95
20040306	07:15:16.28	25.1756	121.5755	3.2	1.22	39	84	−40	134	51	−172
20040312	06:48:31.39	25.1678	121.5407	3.0	1.11	116	67	−20	214	71	−156
20040315	21:22:34.50	25.1731	121.5472	1.5	0.75	269	85	−30	2	60	−174
20040327	17:37:40.28	25.1655	121.5345	3.4	1.56	55	75	−13	149	77	−164
20040402	17:50:37.14	25.1714	121.5435	1.4	1.05	34	56	−53	161	48	−132
20040403	14:30:27.68	25.1759	121.5472	1.3	0.80	249	56	−53	16	48	−132
20040407	14:08:54.31	25.1737	121.5454	1.4	0.82	64	60	−3	156	87	−150
20040512	08:57:54.05	25.1779	121.5705	2.8	1.08	123	71	74	344	25	128
20040528	17:33:36.49	25.1734	121.5444	1.1	0.64	202	51	−8	298	84	−140
20040610	19:42:50.63	25.1725	121.5441	1.4	1.43	24	61	−73	171	33	−118
20041220	14:09:28.14	25.1745	121.5420	1.3	1.03	216	45	−45	341	60	−125

the problem of finding the best fitting stress tensor can be formulated either as a linear least-squares inversion (Michael, 1984), or as a grid search over the stress field parameter space (Gephart and Forsyth, 1984). In either case, the final output will be the orientations of the three principal stress axes (σ_1, σ_2, σ_3) and the parameter R given by

$$R = \frac{\sigma_2 - \sigma_3}{\sigma_1 - \sigma_3} \quad (1)$$

that indicates the relative magnitudes of the stress axes. Each method also calculates the misfit between the best fit model and the data. A high misfit value means that the assumption of a constant stress field in space or time is not valid, hence the stress inversion results may not be meaningful. Hardebeck and Hauksson (2001) tested both the linear inversion and grid search method on a suite of synthetic focal mechanisms containing random errors in order to investigate whether the error estimates of each method accurately reflect the true inversion uncertainty. Their results showed that the linear inversion method is more accurate for noisy datasets and provides more appropriate estimates of uncertainty.

Since our focal mechanisms were derived using a relatively small number of polarities and amplitude ratios we consider them as a noisy dataset and therefore use Michael's method for stress tensor determination. In this method the confidence regions are estimated using a bootstrap technique, where the dataset is resampled with replacement hundreds or thousands of times. In this study we use 2000 bootstrap resamplings which is adequate to produce stable confidence regions up to 95% level (Michael, 1987; Hardebeck and Hauksson, 2001). The average misfit between the best fit model and the data in a single inversion is given by $\overline{\beta}$, the angle between the slip direction and the predicted tangential traction on the fault plane. Michael (1991) estimated the variation of $\overline{\beta}$ as a function of the standard deviation of the errors in strike, dip and rake of the fault plane solutions. From the variation of these parameters in our acceptable solutions we were able to estimate that their standard deviation is of the order of 15° which corresponds to $\overline{\beta}$ equal to 45° (Michael, 1991). This means that stress inversion results with misfits lower than that are considered acceptable and that the stress field is approximately homogeneous.

Initially, we attempted to invert all of the available focal mechanisms in order to check whether a single stress tensor corresponds to our dataset. This resulted in a misfit higher than 45° which implies that the stress field in the TVG area is probably heterogenous and cannot be described by a single stress tensor. Such heterogeneity may be attributed to spatial and/or temporal variations of the stress field in our study area. Unfortunately our dataset is not large enough to investigate possible temporal variations of stress. However, it should be noted that there is no indication (in terms of occurrence of low frequency events, geodetic signals showing aseismic deformation etc) that the conditions around TVG changed during our period of study (e.g. due to magma intrusion). Temporal variations of gas reported during the same period affected only a small area of TVG and were attributed to localized opening of cracks (Lee et al., 2008). It is quite probable therefore that any stress variation is spatial in nature and we accordingly invert subsets of focal mechanisms corresponding to space subvolumes.

First, the focal mechanisms of events deeper than 3 km were inverted and the results showed an acceptable misfit (~37°) and small

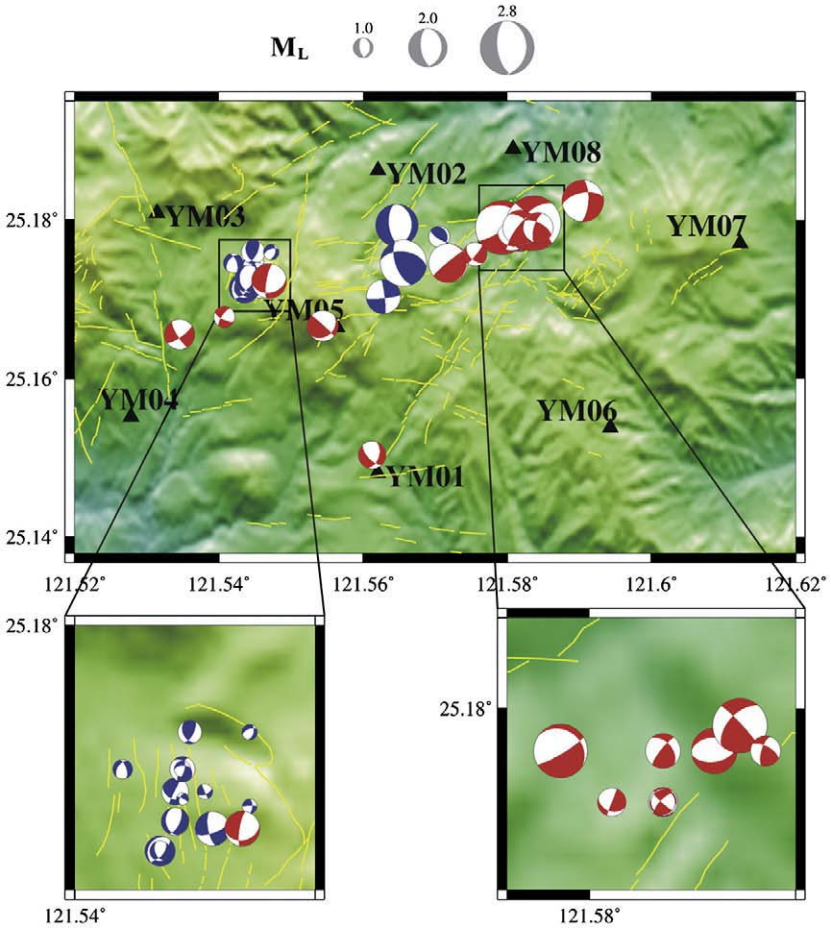

Fig. 6. Map view of the distribution of the 35 focal mechanisms in the TVG area. The different color of the beach balls indicates whether the hypocentral depth is smaller than 3 km (blue), or larger than that (red). The two insets magnify the areas highlighted by the squares. A scale relating the beach ball size to local magnitude is given on top of the plot. For a coloured version of this figure the reader is referred to the web version of the article.

confidence regions. On the contrary, when we tried to invert focal mechanisms of events that occurred shallower than 3 km, we obtained a high misfit and enlarged confidence regions. We also tried to invert separately the focal mechanisms of events occurring beneath the Chihsinshan edifice (events located west of 121.56°E) and the Tayiokeng area (events located east of 121.56°E). For the former, the misfit is acceptable (~44°) but there is some overlap of the confidence regions for σ_1 and σ_2 axes. For the Tayiokeng area the misfit attains a higher value indicating non-uniform stress conditions. We also selected a set of 11 focal mechanisms of events that occurred as swarm activity in the Tayiokeng area in February 16–24, 2004. Inversion results are similar to the ones obtained from the deeper than 3 km events, while the misfit is acceptable (~41°). Fig. 7 shows plots of all these results and Table 3 gives a summary of the azimuth/plunge of the three principal stress axes, R and $\overline{\beta}$ for each subset.

5. Shear wave anisotropy

Shear wave splitting (or seismic birefringence) is the process where shear waves are split into two almost orthogonal polarizations which travel at different velocities (Crampin and Chastin, 2003; Crampin and Peacock, 2005). The mechanism that causes shear wave splitting in the upper crust may be related either to alignment of cracks in response to the *in situ* stress field, or aligned planar features such as fault zone fabrics (Boness and Zoback, 2006). Shear wave data can be used to extract two important splitting parameters, namely the orientation ϕ of the fast moving polarized wave and the time delay δt between the split shear waves. The former provides information about the stress direction while the latter is a measure of the average crack density along the ray paths (e.g., Crampin and Peacock, 2005). Volcanoes are primary areas where seismic anisotropy can be observed, mostly because the upper crust there is pervaded by numerous crack systems generated by magmatic fluid circulation.

For the purpose of investigating shear wave splitting in our dataset we employ the cross-correlation method (Ando et al., 1983). In this method the two horizontal seismograms are rotated in the horizontal plane at a 1° increment of azimuth α from −90° to 90°. Then for each azimuth the cross-correlation coefficient C is calculated between the two orthogonal seismograms, for a range of time delays τ in a selected time window. When the absolute value of C reaches a maximum the corresponding values of α and τ are chosen as the fast polarization direction and the time delay of the slow shear wave respectively. The measurement uncertainty for a 95% confidence interval is estimated using a t-test for the values of C in the way described by Kuo et al. (1994). Waveforms can be distorted by phase conversions in the case when they reach the surface at incidence angles larger than a critical value given by $\sin^{-1}(V_s/V_p)$, where V_s and V_p is the S-/P-wave velocities respectively. The critical angles for our minimum 1D velocity model range from about 33° in the first 3 km to 35° at larger depths. We again use the short-period waveforms of the 144 high frequency events and select event-station pairs that correspond to incidence angles that are smaller than the critical ones.

The seismograms were first interpolated to 200 samples s^{-1}, integrated to displacement and then bandpass filtered between 1–10 Hz using a two-pole Butterworth filter. The measurement window for each waveform is defined in the following way: the start of the

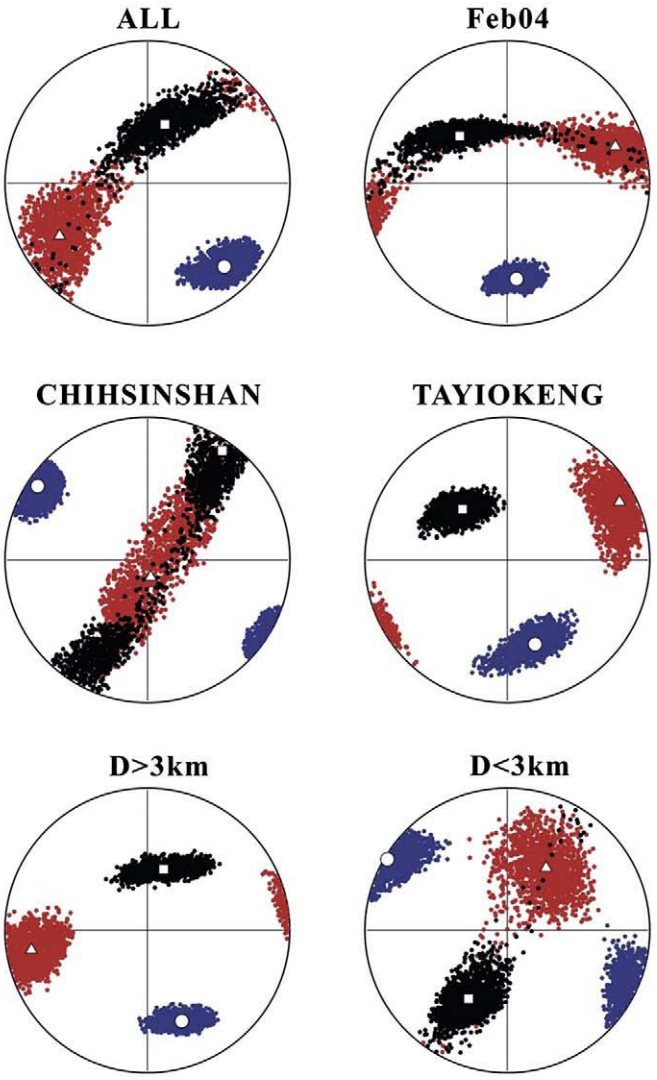

Fig. 7. Lower hemisphere projections of the directions of the principal stress axes obtained from the datasets listed in Table 3 (see also text for more details). The square represents the σ_1 axis, the circle signifies the σ_3 and the triangle the σ_2 axis. The colored dots define the 95% confidence region of each stress axis. For a coloured version of this figure the reader is referred to the web version of the article.

window is fixed 0.05 s before the S-wave arrival while the endpoint is adjusted each time until the value of C between the fast and slow components becomes maximum. The reasoning behind this choice of window measurement is based on the fact that the suitable endpoint may actually vary with different waveform characteristics. Following Liu et al. (2008) we consider that a splitting measurement is valid only when it conforms to these criteria: (a) the C value is larger than 0.80, (b) the signal-to-noise ratio is larger than 3, (c) the change of the measured δt is less than 0.02 s when the window size is varied by ± 0.02 s, and (d) the change of the measured ϕ is less than 10° when the window size is varied by ± 0.02 s. In this way we were able to extract 50 splitting parameters and Fig. 8a, b shows examples of valid splitting measurements. These shear wave splitting observations may also be attributed to other processes such as complex source mechanisms, or S-to-P conversions. The small magnitude of the analyzed events and the simplicity of the recorded waveforms give us confidence that the former explanation is unlikely in our case. The latter explanation does not seem to be probable either, since this type of conversion shows the greatest amplitude on the vertical component, unlike our data that exhibit the maximum amplitude on the horizontal component.

Table 3
Summary of stress inversion results for the different datasets mentioned in the text.For each stress axes (σ_1, σ_2, σ_3) the resulting azimuth and plunge is given along with the value of R and the misfit angle $\overline{\beta}$. Nobs is the number of focal mechanisms used in each stress inversion.

Dataset	Nobs	σ_1	σ_2	σ_3	R	$\overline{\beta}$
ALL	35	16°/54°	239°/28°	138°/20°	0.6	58°
$D>3$ km	17	15°/53°	260°/17°	159°/32°	0.5	37°
$D<3$ km	18	210°/43°	32°/47°	300°/1°	0.5	52°
Tayiokeng	17	318°/50°	63°/12°	162°/37°	0.4	48°
Chihsinshan	18	34°/7°	170°/80°	310°/7°	0.8	44°
Feb04	11	314°/51°	71°/20°	174°/32°	0.7	42°

Table 4 summarizes all the results for each station in terms of number of observations, the median value for ϕ, average value of δt, its standard deviation and the average anisotropy percentage ξ that is calculated by (Savage et al., 1990)

$$\xi = \left(\frac{\delta t}{R} * V_s\right) \times 100\% \quad (2)$$

where R is the hypocentral distance in km and V_s is the S-wave velocity at the focal area. Except from station YM07 where no valid measurement could be found and station YM04 that has only two valid measurements, all other stations have at least 4 pairs of splitting parameters. The average delay times range from 83.7 to 16.6 ms while the largest values are observed at the stations around Chihsinshan (YM01, YM02, YM03, YM05). Fig. 9 combines the fracture lineations derived from LiDAR data and the fast polarization directions resulting from the shear wave splitting measurements.

6. Discussion

6.1. Regional versus local stress field

Geodetic and geologic observations provide most of the information we have about the regional stress field orientation in northern Taiwan (Yu et al., 1997; Hu et al., 2001; Bos et al., 2003; Chang et al., 2003). These studies indicate the presence of extensional deformation in the NW–SE direction of the order of 2–16 mm yr^{-1}. Such a deformation style confirms earlier suggestions that the northern extent of Taiwan's mountain belt is subject to gravitational collapse due to the opening of the Okinawa Trough (Teng, 1996). Even though shallow seismicity in northern Taiwan is in general low, the few earthquake observations that are available seem to agree with the geodetic results. Focal mechanisms of events that occur along the Okinawa Trough, derived from the inversion of regional waveforms, show normal faulting with N–S extension that progressively becomes NW–SE for events located closer to Taiwan (Kao and Jian, 2001). Stress inversions of small samples of focal mechanisms (Yeh et al., 1991) or slickenside data (Chu et al., 1998) indicate a subvertical σ_1 while σ_3 has a NW–SE direction and is close to the horizontal.

Our stress inversion results for the TVG area partly agree with the orientation of the regional stress field described previously. The stress tensor that corresponds to focal mechanisms of events located deeper than 3 km shows vertical compression, while extension is orientated along the SE direction. This stress field is also similar to the stress tensor that resulted from the inversion of focal mechanisms of the events that occurred during February 2004 near Tayiokeng. On the other hand, the stress field around Chihsinshan deviates from the regional one since our results suggest that σ_1 is almost horizontal. This implies the predominance of horizontal stresses beneath this area that would favour the opening of cracks and the ascent and circulation of hydrothermal fluids. This suggestion is also supported by the occurrence of strong fumarolic activity, spasmodic bursts and mixed frequency events near the Chihsinshan edifice. Our results also

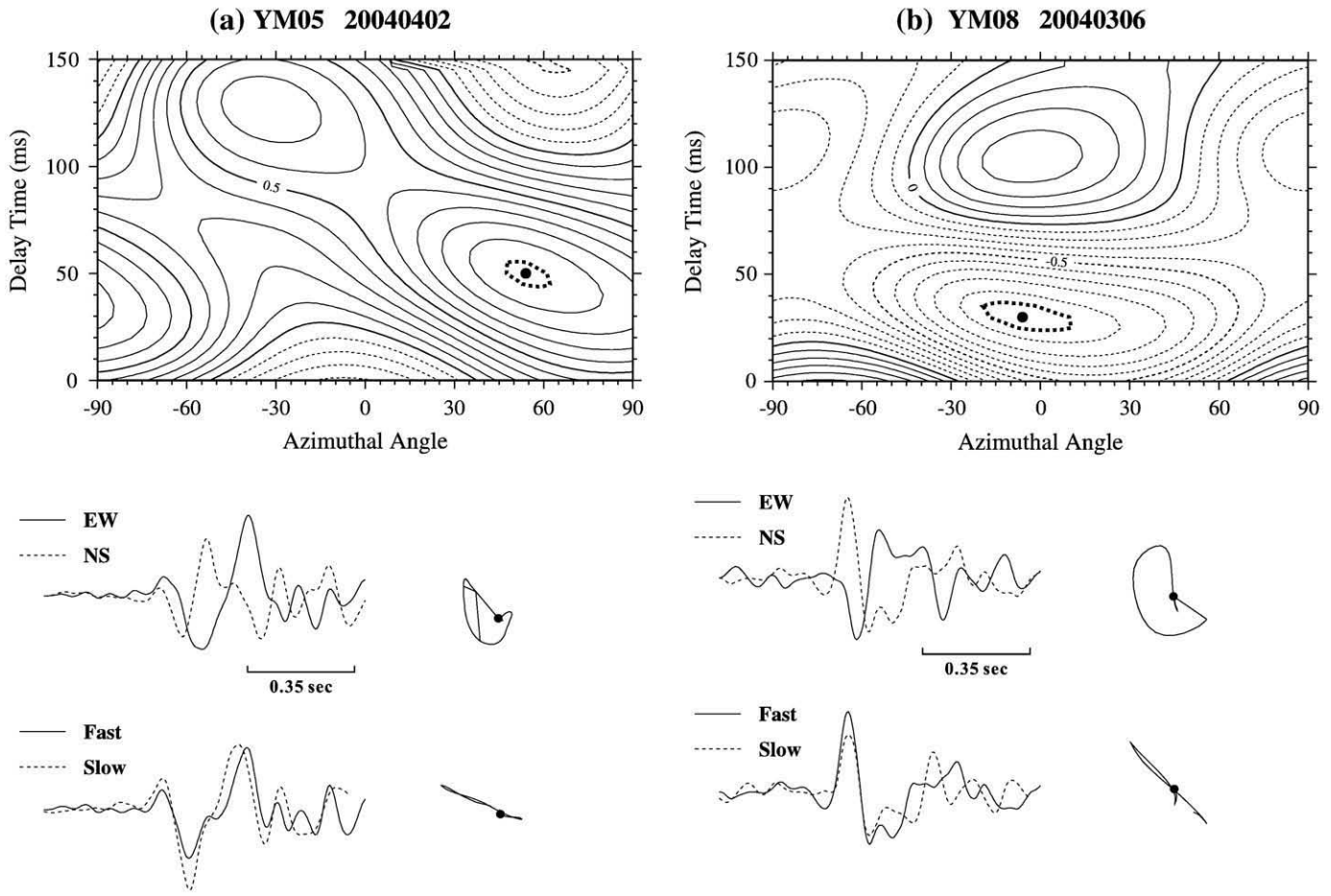

Fig. 8. (a) A valid splitting measurement of an S-wave recorded at station YM05 for an event that occurred in April 2, 2004. Upper panel: diagram of the distribution of the cross-correlation coefficient in (ϕ, δt) space. The preferred solution corresponding to the maximum value (dot) is shown within the 95% confidence region (thick dashed line); dashed contours represent negative coefficients. Lower panel: upper two traces are the superposition of E–W and N–S components, while the lower two traces are the corrected fast and slow components. Particle motions are shown to the right of each sub-panel, (b) a valid splitting measurement of an S-wave recorded at station YM08 for an event that occurred in March 6, 2004; symbols are the same as in (a).

indicate that as a whole, the shallow crust beneath TVG clearly exhibits stress heterogeneity as shown by the high misfit for the stress inversion of shallower than 3 km focal mechanisms. Indeed, such a stress pattern agrees with similar findings for the shallow parts of other active volcanoes like Mt Etna (Cocina et al., 1997, 1998).

6.2. Anisotropy and crack orientation

The shear wave splitting measurements presented in this study complement the stress inversion results in two ways. First, the median of the fast polarization directions in most stations is NNE to NE which coincides with the strike of the major fracture system in the TVG area and with the σ_1 direction around Chihsinshan. The only station that seems to deviate from this pattern is YM06 that follows some secondary ESE fracture lineations rather than the main fracture system. These observations can be interpreted as an indication that the observed splitting is caused by cracks that are aligned almost parallel to the maximum stress direction. Second, the delay time measurements when plotted against earthquake focal depth show that most splitting corresponds to sources deeper than 2.5 km (Fig. 10). Such a pattern suggests that the region that is anisotropic extends only through the upper 2.5 km of the TVG area crust. This top layer exhibits a high V_p/V_s ratio (~1.79) and is also the place where most of the spasmodic burst events are located. These observations show that the shallow crust beneath TVG is pervaded by a dense network of fluid-saturated cracks and also agree well with the stress inversion results that reveal non-uniform stress conditions in the upper 3 km. The average percentage of shear wave velocity anisotropy stemming from our measurements is 2.9% which is comparable to values found in other geothermal or volcanic areas such as the Geysers area in California (Evans et al., 1995), or the Hengill triple junction in Iceland (Evans et al., 1996). The fact that three stations around Chihsinshan exhibit average percentages in excess of 5% provides additional evidence that the crust there is heavily cracked and has probably reached fracture criticality (Crampin and Peacock, 2005).

Table 4
Summary of the shear-wave splitting measurements for the TVG dataset. Nobs denotes the number of observations, $\overline{\phi}$ is the median of the fast polarization directions while $\overline{\delta t}$ and $\sigma_{\delta t}$ are the average delay time and standard deviation in each station respectively. The last column represents the average percentage of shear wave velocity anisotropy (ξ) in each station.

Station	Nobs	$\overline{\phi}$	$\overline{\delta t}$ (ms)	$\sigma_{\delta t}$ (ms)	ξ
YM01	4	N17°E	83.7	20.1	5.70
YM02	5	N55°E	62.0	32.5	5.42
YM03	4	N62°E	82.5	32.7	6.59
YM04	2	N60°E	22.5	10.6	1.92
YM05	6	N52°E	42.5	26.2	3.65
YM06	6	N72°W	16.6	2.5	0.81
YM08	23	N39°E	20.0	9.2	1.64

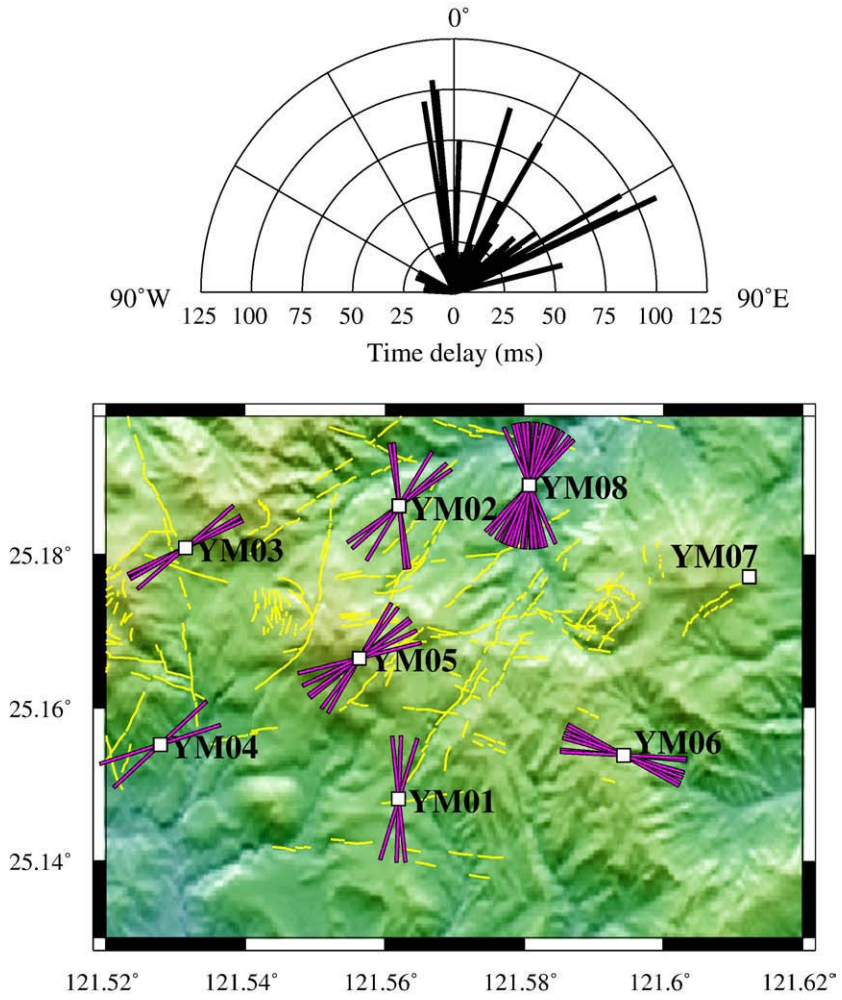

Fig. 9. Upper panel: windrose diagram of the fast polarization directions as a function of delay time for the 50 splitting measurements. Lower panel: map showing the polarization directions of the fast shear wave as measured at each station (see also Table 4). The yellow lines are the surface fractures in the TVG area derived from LiDAR data. For a coloured version of this figure the reader is referred to the web version of the article.

6.3. Volcanotectonic earthquakes at TVG

Classification schemes for volcanic earthquakes mainly follow two different methodologies of assigning events into specific groups. The first has to do with *a priori* assumptions about the source process that may be responsible for the generation of the volcanoseismic signal. The second is more general and uses the overall signal characteristics in the time and frequency domains without assuming anything about

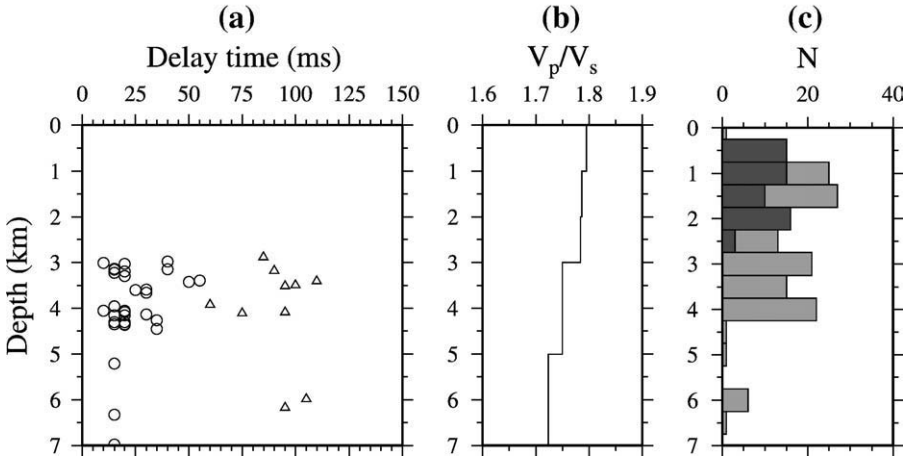

Fig. 10. (a) Diagram showing the distribution of delay times (δt) versus focal depth for all the valid splitting measurements (see also Table 4). Delay times that correspond to an anisotropy percentage greater than 5% are plotted as triangles, while those less than that are shown as circles; (b) the distribution of the V_p/V_s ratio as a function of depth stemming from the minimum 1D velocity velocity model; (c) histogram showing the depth distribution of located high frequency earthquakes (gray bars) and events belonging to spasmodic bursts (black bars).

the underlying source process. According to the first approach earthquakes that occur near volcanoes but are similar to tectonic ones should be termed 'volcanotectonic' and are produced by brittle fracture of rock along a fault plane caused by volcanic processes (e.g. Lahr et al., 1994). The second approach would term such events as high frequency events due to their frequency content. Moran (2003) has suggested that high frequency events that are generated as a response to the regional stress field are ordinary tectonic earthquakes and should not be labeled volcanotectonic. On the contrary, events that are generated by a stress field that is local around a particular volcano are the ones that are most likely linked to volcanic processes. In this sense, the events around Chihsinshan are true volcanotectonic events since they correspond to a stress tensor different than the regional one and occur at an area where fluid circulation is particularly intense, as demonstrated by our observations. This indicates that the magmatic system beneath the Chihsinshan edifice can be considered active and a potential site for future eruptive activity at TVG.

Acknowledgements

We would like to thank the National Science Council of Taiwan and the National Yangmingshan Park for the financial support of this research. Comments from two anonymous reviewers and the Editor-in-Chief Prof. Lionel Wilson, helped in clarifying several aspects of our analysis.

References

Ando, M., Ishikawa, Y., Yamazaki, F., 1983. Shear wave polarization anisotropy in the upper mantle beneath Honshu, Japan. J. Geophys. Res. 88, 5850–5864.
Bianco, F., Castellano, M., Milano, G., Ventura, G., Vilardo, G., 1998. The Somma-Vesuvius stress field induced by regional tectonics: evidences from seismological and mesostructural data. J. Volcanol. Geotherm. Res. 82, 199–218.
Boness, N., Zoback, M., 2006. A multiscale study of the mechanism controlling shear velocity anisotropy in the San Andreas Fault Observatory at Depth. Geophysics 71, F131–F146.
Bos, A., Spakman, W., Nyst, M.C.J., 2003. Surface deformation and tectonic setting of Taiwan inferred from a GPS velocity field. J. Geophys. Res. 108. doi:10.1029/2002JB002336.
Chan, Y.C., Chen, Y.G., Shin, T.Y., Huang, C., 2007. Characterizing the Hsincheng active fault in northern Taiwan using airborne LiDAR data: detailed geomorphic features and their structural implications. J. Asian Earth Sci. 31. doi:10.1016/j.jseaes.2006.07.029.
Chang, C.P., Chang, T.Y., Angelier, J., Kao, H., Lee, J.C., Yu, S.B., 2003. Strain and stress field in Taiwan oblique convergent system: constraints from GPS observation and tectonic data, Earth Planet. Sci. Lett. 214. doi:10.1016/S0012-821X(03)00360-1.
Chen, C.H., Lin, S.B., 2002. Eruptions younger than 20 ka of the Tatun volcano group as viewed from the sediments of the Sungshan formation in the Taipei basin. West. Pac. Earth Sci. 2, 191–204.
Chen, K.J., Lin, C.H., Hsieh, C.J., 2002. Mapping seismic attenuation structures of the volcanic area in northern Taiwan. West. Pac. Earth Sci. 2, 273–290.
Chu, C.J., Lee, C.T., Teng, L.S., 1998. Structural features and Quarternary tectonics of the Chinshan fault, northern Taiwan. J. Geol. Soc. China 41, 25–42.
Cocina, O., Neri, G., Privitera, E., Spampinato, S., 1997. Stress tensor computations in the mount Etna area (southern Italy) and tectonic implications. J. Geodyn. 23, 109–127.
Cocina, O., Neri, G., Privitera, E., Spampinato, S., 1998. Seismogenic stress field beneath Mt Etna (south Italy) and possible relationships with volcanotectonic features. J. Volcanol. Geotherm. Res. 83, 335–348.
Crampin, S., Chastin, S., 2003. A review of shear wave splitting in the crack-critical crust. Geophys. J. Int. 155, 221–240.
Crampin, S., Peacock, S., 2005. A review of shear wave splitting in the compliant crack-critical anisotropic Earth. Wave Motion 41. doi:10.1016/j.wavemoti.2004.05.006.
Evans, J.R., Julian, B.R., Foulger, G.R., Ross, A., 1995. Shear-wave splitting from local earthquakes at The Geysers geothermal field, California. Geophys. Res. Lett. 22, 501–504.
Evans, J.R., Foulger, G.R., Julian, B.R., Miller, A.D., 1996. Crustal shear-wave splitting from local earthquakes in the Hengill triple junction, southwest Iceland. Geophys. Res. Lett. 23, 455–458.
Gephart, J.W., 1990. FMSI: A FORTRAN program for inverting fault/slickenside and earthquake focal mechanism data to obtain the regional stress tensor. Comput. Geosci. 16, 953–989.
Gephart, J.W., Forsyth, D.W., 1984. An improved method for determining the regional stress tensor using earthquake focal mechanism data: application to the San Fernando earthquake sequence. J. Geophys. Res. 89, 9305–9320.
Hardebeck, J.L., Hauksson, E., 2001. Stress orientations obtained from earthquake focal mechanisms: what are appropriate uncertainty estimates? Bull. Seismol. Soc. Am. 91, 250–262.
Hardebeck, J.L., Shearer, P.M., 2003. Using S/P amplitude ratios to constrain the focal mechanisms of small earthquakes. Bull. Seismol. Soc. Am. 93, 2434–2444.
Hu, J.C., Yu, S.B., Angelier, J., Chu, H.T., 2001. Active deformation of Taiwan from GPS measurements and numerical simulations. J. Geophys. Res. 106, 2265–2280.
Kao, H., Jian, P.R., 2001. Seismogenic patterns in the Taiwan region: insights from source parameter inversion of BATS data. Tectonophysics 333, 179–198.
Kim, K.H., Chang, C.H., Ma, K.F., Chiu, J.M., Chen, K.C., 2005. Modern seismic observations in the Tatun volcano region of northern Taiwan: seismic/volcanic hazard adjacent to the Taipei metropolitan area. Terr. Atm. Ocean. Sci. 16, 579–594.
Konstantinou, K.I., Lin, C.H., Liang, W.T., 2007. Seismicity characteristics of a potentially active Quaternary volcano: the Tatun Volcano group, northern Taiwan. J. Volcanol. Geotherm. Res. 160. doi:10.1016/j.jvolgeores.2006.09.009.
Kuo, B.Y., Chen, C.C., Shin, T.C., 1994. Split S waveforms observed in northern Taiwan: implications for crustal anisotropy. Geophys. Res. Lett. 21, 1491–1494.
Lahr, J.C., Chouet, B.A., Stephens, C.D., Power, J.A., Page, R.A., 1994. Earthquake classification, location, and error analysis in a volcanic environment: implications for the magmatic system of the 1989–1990 eruptions at Redoubt Volcano, Alaska. J. Volc. Geotherm. Res. 62, 137–151.
Lee, H.F., Yang, T.F., Lan, T.F., Chen, C.H., Song, S.R., Tsao, S., 2008. Temporal variations in gas compositions of fumaroles in the Tatun Volcano Group, northern Taiwan. J. Volcanol. Geotherm. Res. 178. doi:10.1016/j.jvolgeores.2008.06.005.
Legrand, D., Calahorrano, A., Guillier, B., Rivera, L., Ruiz, M., Villagómez, D., Yepes, H., 2002. Stress tensor analysis of the 1998–1999 tectonic swarm of northern Quito related to the volcanic swarm of Guagua Pichincha volcano, Ecuador. Tectonophysics 344, 15–36.
Lin, C.H., Konstantinou, K.I., Liang, W.T., Pu, H.C., Lin, Y.M., You, S.H., Huang, Y.P., 2005. Preliminary analysis of volcanoseismic signals recorded at the Tatun volcano group, northern Taiwan. Geophys. Res. Lett. 32, L10313. doi:10.1029/2005GL022861.
Liu, Y., Zhang, H., Thurber, C., Roecker, S., 2008. Shear wave anisotropy in the crust around the San Andreas fault near Parkfield: spatial and temporal analysis. Geophys. J. Int. 172. doi:10.1111/j.1365-246X.2007.03618.x.
Lomax, A., Virieux, J., Volant, P., Berge-Thierry, C., 2000. Probabilistic earthquake location in 3D and layered models. In: Thurber, Rabinowitz (Ed.), Advances in seismic event location, pp. 101–134.
Michael, A.J., 1984. Determination of stress from slip data: faults and folds. J. Geophys. Res. 89, 11517–11526.
Michael, A.J., 1987. Use of focal mechanisms to determine stress: a control study. J. Geophys. Res. 92, 357–368.
Michael, A.J., 1991. Spatial variations in stress within the 1987 Whittier Narrows, California, aftershock sequence: new techniques and results. J. Geophys. Res. 96, 6303–6319.
Miller, A.D., Foulger, G.R., Julian, B.R., 1998. Non-double-couple earthquakes 2. Observations. Rev. Geophys. 36, 551–568.
Moran, S.C., 2003. Multiple seismogenic processes for high frequency earthquakes at Katmai national park, Alaska: evidence from stress tensor inversions of fault plane solutions. Bull. Seismol. Soc. Am. 93, 94–108.
Park, J.C., Kim, W., Chung, T.W., Baag, C.E., Ree, J.H., 2007. Focal mechanisms of recent earthquakes in the Southern Korean peninsula. Geophys. J. Int. 169. doi:10.1111/j.1365-246X.2007.03321.
Rau, R.J., Wu, F.T., Shin, T.C., 1996. Regional network focal mechanism determination using 3D velocity model and SH/P amplitude ratio. Bull. Seismol. Soc. Am. 86, 1270–1283.
Roman, D., Moran, S.C., Power, J.A., Cashman, K.V., 2004. Temporal and spatial variation of local stress fields before and after the 1992 eruptions of Crater Peak vent, Mount Spurr volcano, Alaska. Bull. Seismol. Soc. Am. 94, 2366–2379.
Savage, M.K., Peppin, W.A., Vetter, U.R., 1990. Shear wave anisotropy and stress direction in and near Long Valley caldera, California, 1979–1988. J. Geophys. Res. 95, 11165–11177.
Snoke, J.A., Munsey, J.W., Teague, A.G., Bollinger, G.A., 1984. A program for focal mechanism determination by combining use of polarity and SV-P amplitude ratio data. Earthq. Notes 55 (3), 15.
Song, S.R., Yang, T.F., Yeh, Y.H., Tsao, S.J., Lo, H.J., 2000. The Tatun volcano group is active or extinct? J. Geol. Soc. China 43, 521–534.
Teng, L.S., 1996. Extensional collapse of the northern Taiwan mountain belt. Geology 24, 949–952.
Tsai, Y.B., 1986. Seismotectonics of Taiwan. Tectonophysics 125, 17–38.
Waldhauser, F., Ellsworth, W.L., 2000. A double-difference earthquake location algorithm: method and application to the northern Hayward fault, California. Bull. Seismol. Soc. Am. 90, 1353–1368.
Wang, K.L., Chung, S.L., Chen, C.H., Shinjo, R., Yang, T.F., Chen, C.H., 1999. Post-collisional magmatism around northern Taiwan and its relation with opening of the Okinawa trough. Tectonophysics 308, 363–376.
Wu, F.T., Rau, R.J., Salzberg, D., 1997. Taiwan orogeny: thin-skinned or lithospheric collision? Tectonophysics 274, 191–220.
Yang, T.F., Sano, Y., Song, R.S., 1999. $^{3}He/^{4}He$ ratios of fumaroles and bubbling gases of hot springs in Tatun volcano group, north Taiwan. Nuovo Cim. 22, 281–285.
Yeh, Y.H., Barrier, E., Lin, C.H., Angelier, J., 1991. Stress tensor analysis in the Taiwan area from focal mechanisms of earthquakes. Tectonophysics 200, 267–280.
Yeh, Y.H., Liu, C.C., Lin, C.H., Liu, C.C., Yen, H.Y., 1998. Geophysical monitoring of volcano activities at Mt. Tatun. Eos Trans. AGU 79 (24) Westrn Pac. Geophys. Meet. Suppl., W124.
Yu, S.B., Chen, H.Y., Kuo, L.C., Lallemand, S.E., Tsien, H.H., 1997. Velocity field of GPS stations in the Taiwan area. Tectonophysics 274, 41–59.